ACS APPLIED MATERIALS & INTERFACES

Research Article

www.acsami.org

Gadolinium-Based $CuInS_2$/ZnS Nanoprobe for Dual-Modality Magnetic Resonance/Optical Imaging

Chun-Yi Cheng,[‡,†] Keng-Liang Ou,[‡,‡,§,⊥,#] Wei-Ting Huang,[†] Jem-Kun Chen,[‖] Jia-Yaw Chang,*[,†] and Cheng-Hsien Yang*[,△]

[†]Department of Chemical Engineering, National Taiwan University of Science and Technology, Section 4, #43, Keelung Road, Taipei 106, Taiwan, Republic of China

[‡]Research Center for Biomedical Devices and Prototyping Production, Taipei Medical University, Taipei 110, Taiwan, Republic of China

[§]Research Center for Biomedical Implants and Microsurgery Devices and [⊥]Department of Biomedical Materials and Tissue Engineering, College of Oral Medicine, Taipei Medical University, 250 Wu Hsing Street, Taipei 110, Taiwan, Republic of China

[#]Department of Dentistry, Taipei Medical University-Shuang-Ho Hospital, Taipei 235, Taiwan, Republic of China

[‖]Department of Materials Science and Engineering, National Taiwan University of Science and Technology, Taipei, Taiwan, Republic of China

[△]ShiFeng Technology Co., Ltd. Tainan 709, Taiwan, Republic of China

Ⓢ *Supporting Information*

ABSTRACT: A new magnetic resonance/optical nanoprobe with specific cellular targeting capabilities based on nontoxic $CuInS_2$/ZnS quantum dots (QDs) with direct covalent attachment of a Gd(III)-complex for tumor-specific imaging is reported. We introduce amphiphilic poly(maleic anhydride-alt-1-octadecene) to interdigitate with hydrophobic, protective agents on the surface of $CuInS_2$/ZnS QDs that allows phase transfer of hydrophobic QDs from the organic into aqueous phase. Carbodiimide chemistry is used to covalently couple the Gd(III) complex on the surface of $CuInS_2$/ZnS QDs, and then folic acid is further utilized to functionalize this dual-modality nanoprobe for active tumor targeting based on the fact that the membrane-associated folate receptor is overexpressed in many tumor cells. The longitudinal relaxivity value is 3.72 mM^{-1} s^{-1} for the dual-modality nanoprobe and a clear, positive, and increasing contrast enhancement of magnetic resonance signals concurrently with increasing Gd(III) concentration is observed. The dual-modality nanoprobe exhibits negligible cytotoxicity with >80% cell viability at a concentration of up to 100 μg/mL in human cervical (HeLa), human liver carcinoma (HepG2), and human breast (MCF-7) cells after 24 h. The specificity of folic-acid-conjugated nanoprobe cellular uptake has been investigated by confocal scanning laser imaging, which revealed that HeLa cells, expressing the folate receptor, internalized a higher level of dual-modality nanoprobes than HepG2 and MCF-7 cells.

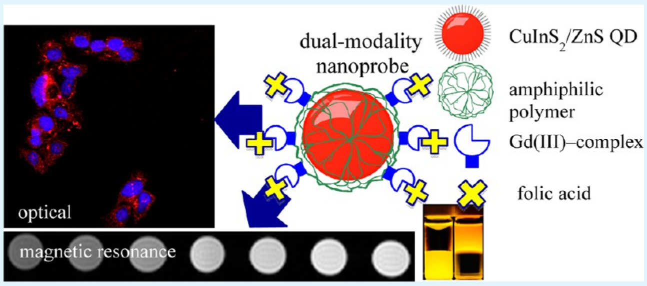

KEYWORDS: *$CuInS_2$/ZnS, Gd(III)-complex, optical imaging, magnetic resonance imaging*

1. INTRODUCTION

Noninvasive imaging is crucial toward increasing the selectivity and sensitivity of early stage cancer diagnosis and therapy. Among the various imaging technologies, magnetic resonance (MR) imaging is a powerful, noninvasive diagnostic tool, which offers advantages such as high spatiotemporal resolution, no exposure to radiation, noninvasiveness, impressive anatomic resolution and tissue penetration, and high-resolution images of the entire body with exquisite image contrast.[1] The creation of MR imaging depends primarily on the response of proton spin−spin relaxation in the presence of an external magnetic field when triggered with a radio frequency pulse. This radio frequency pulse shifts the direction of the magnetization vector away from the axial field, and intrinsic longitudinal (T_1) and transverse (T_2) relaxation times of distinct regions of tissues and organs result in a variation of the MR signal intensity.[2,3] Typical contrast agents for MR imaging act to shorten the T_1/T_2 relaxation times of nearby water protons and provide brighter/positive and darker/negative images where they are accumulated. T_1-weighted MR agents offer brighter/positive contrast enhancement, which can greatly help to identify pathogenic or biological conditions of the tissues where they accumulate, and are quite frequently used in clinical disease diagnosis.[4,5] Of the different positive contrast agents,

Received: February 20, 2013
Accepted: April 25, 2013
Published: April 25, 2013

dx.doi.org/10.1021/am401428n | *ACS Appl. Mater. Interfaces* 2013, 5, 4389−4400

gadolinium ion (Gd(III)), a type of paramagnetic metal ion with seven unpaired electrons in its 4f orbital, is widely used as a T_1-weighted MR agent, and has the ability to brighten MR images by greatly shortening the longitudinal relaxation time (T_1) of surrounding water protons. Unfortunately, Gd(III)-complexes generally have a short circulating time because of rapid excretion through urine, which hampers high-resolution imaging requiring extended scanning times. Despite its attractive properties, sensitivity of MR imaging is relatively poor for low levels of molecular targets and suffers from a lack of cell specificity compared to other imaging modalities. On the other hand, optical imaging has excellent sensitivity at subcellular levels and for quantifying molecular events, but its limited capability in examining deep tissues restricts collection of information in vivo. Therefore, a single nanoprobe, useful for both MR and optical imaging, would lead to novel tools for research and life science because of the highly complementary capabilities of the two imaging technologies. The use of a single nanoprobe with both imaging techniques minimizes artifacts and enables significant improvement in diagnostic accuracy and therapeutic strategy, in comparison with standalone imaging.[6]

In searching for new imaging agents integrated with different modalities, quantum dots (QDs) have drawn much attention as a convenient scaffold. QDs exhibit discrete atomiclike energy levels and unique optical properties that depend critically on both particle size and the particle surface chemistry. They have received considerable attention in diagnostic, molecular, and subcellular imaging because of their narrow emission with broad excitation property, multicolor excitation with large extinction coefficients ($\sim 1 \times 10^5$ M^{-1} cm^{-1}), and high resistance to photobleaching as compared to organic dyes. Thus, the integration of T_1-type MR imaging agents with QDs would be highly desirable. A recent example features the synthesis of Gd(III)-functionalized CdS:Mn/ZnS,[7] CdSeTe/ZnS,[8] CdSe,[6,9–13] and CdTe/ZnS[14] QDs. However, the intrinsic toxicity of such cadmium-containing QDs cannot be ignored because they easily disintegrate in biological systems, causing leakage of cadmium ions as well as heavy-metal accumulation in subcellular regions, and might actually cause the extinction of biological systems. For the sake of the environment, an increasing number of researchers are now integrating green chemistry principles into their synthetic methods, which not only makes the final products greener but also minimizes the quantity of hazardous starting materials that are employed in their manufacture. This has motivated the search for alternative semiconducting materials that are not only technologically useful but also environmentally benign. In recent developments, I–III–VI ternary semiconductors (such as $CuInS_2$[15–20]) have been considered to be potential candidates as they are not only cadmium free but also provide high extinction coefficients and photoluminesence (PL) emission ranging from the visible to the NIR. These materials represent an emerging new generation of luminescent QDs, and many of their properties and possible uses have yet to be investigated. Even the application of I–III–VI QDs in bioimaging is in the beginning stages.

Moreover, tumor-specific imaging is another issue that must be addressed in tumor diagnosis. A deficiency of specificity for target tissues or organs is among the greatest hindrance in improving the precision and accuracy of early diagnosis and determination of tumor anatomical structure as well as metabolism. It is not efficient to deliver nanoprobes by accumulation in tumor tissues only through passive targeting via the enhanced permeability and retention effect.[21,22] Active targeting can effectively deliver nanoprobes directly to the desired target cells. The use of a multiple-modality nanoprobe with active targeting for early detection and diagnosis is expected to minimize artifacts and enable significant improvements in diagnostic accuracy and therapeutic strategy that cannot be achieved with the individual constituents. Although the use of I–III–VI QDs as a platform for optical imaging has already been reported in the literature,[15,20,23–28] to the best of our knowledge, multifunctional I–III–VI QDs simultaneously exhibiting magnetic resonance/optical imaging and targeting capability have not been reported.

In the present study, we report a new MR/optical nanoprobe based on nontoxic $CuInS_2$/ZnS QDs with direct covalent attachment of a Gd(III)-complex. Folic acid was also covalently tethered on this dual-modality nanoprobe for active tumor targeting. To assess the effectiveness of the proposed dual-modality nanoprobe as an MR imaging contrast agent, the magnetic resonance relaxivity of the dual-modality nanoprobe was measured using a clinical MR scanner at room temperature. By using confocal scanning laser imaging characterization, we demonstrate that the dual-modality nanoprobe can target cells specifically and effectively via folate-receptor-mediated targeted delivery.

2. EXPERIMENTAL SECTION

2.1. Materials. Copper acetate (CuAc, 97%), zinc stearate (90%), potassium ethylxanthate (96%), zinc chloride (98%), 1-dodecanethiol (DDT, 97%), 1-octadecene (ODE, 90%), 3-(4,5-dimethylthiazol-2-yl)-2,5-diphenyltetrazolium bromide (MTT, 97.5%), and 4′-6-diamidino-2-dihydrochloride (DAPI, >98%), nonessential amino acid solution (100×), sodium pyruvate (100 mM), minimum essential eedium eagle, L-glutamine (200 mM), antibiotic antimycotic solution (100X), trypsin-EDTA solution (0.25%), sodium bicarbonate (99.5–100.5%), diethylenetriaminepentaacetic acid gadolinium(III) dihydrogen salt hydrate (Gd(III)–DTPA, 97%), and ethylenediamine were purchased from Sigma-Aldrich (Milwaukee, WI, USA). 1-Dodecanethiol (98%) and 1-octadecene (ODE, 90%) were purchased from Acros Organics. Indium acetate (InAc, 99.99%), and n-ethyl-N′-(3-dimethylamino-propyl) carbodiimide (EDC, 98%) was purchased from Alfa-Aesar (Ward Hill, MA, USA). Poly(maleic anhydride-alt-1-octadecene) (PMO, M_n = 30 000–50 000) and N-hydroxysuccinimide (NHS, >95%) was purchased from Thermo Scientific (Rockford, USA). Folic acid (>98%) was purchased from T.C.I. Chemical Co. (TCI, Japan). All chemicals were used directly without further purification.

2.2. Preparation of $CuInS_2$/ZnS QDs. $CuInS_2$/ZnS QDs were prepared according to our previously published procedure.[29] CuAc (0.2 mmol), InAc (0.6 mmol), DDT (10 mmol), and 5 mL of ODE were loaded into a reaction vessel equipped with a condenser, a magnetic stirring bar and a thermometer with an attached Schlenk line. The mixture was degassed under vacuum, purged three times with argon, and heated at 40 °C for 1 h. The resulting solution was subsequently heated to 240 °C. The injection solution of the ZnS precursor was prepared by mixing 9 mL of zinc stearate (0.267 M) in ODE and 3 mL of zinc ethylxanthate (0.1 M) in toluene containing 300 μL of dimethylformamide. ZnS precursors were added dropwise by means of a syringe pump (KD Scientific KDS100, USA) for 30 min once the temperature reached 240 °C. After the injection was complete, the reaction mixture was cooled to room temperature, followed by centrifugation at 6000 rpm for 20 min. The precipitate was then discarded and the supernatant was added into 5 mL of chloroform. The obtained solution precipitated by adding 7.5 mL of methanol and further purified by repeated centrifugation and decantation.

2.3. Preparation of PMO Polymer-Coated $CuInS_2$/ZnS QDs (QD@PMO–COOH). $CuInS_2$/ZnS QDs (12 mg) and PMO polymers (25 mg) were mixed in 20 mL of chloroform. The reaction mixture

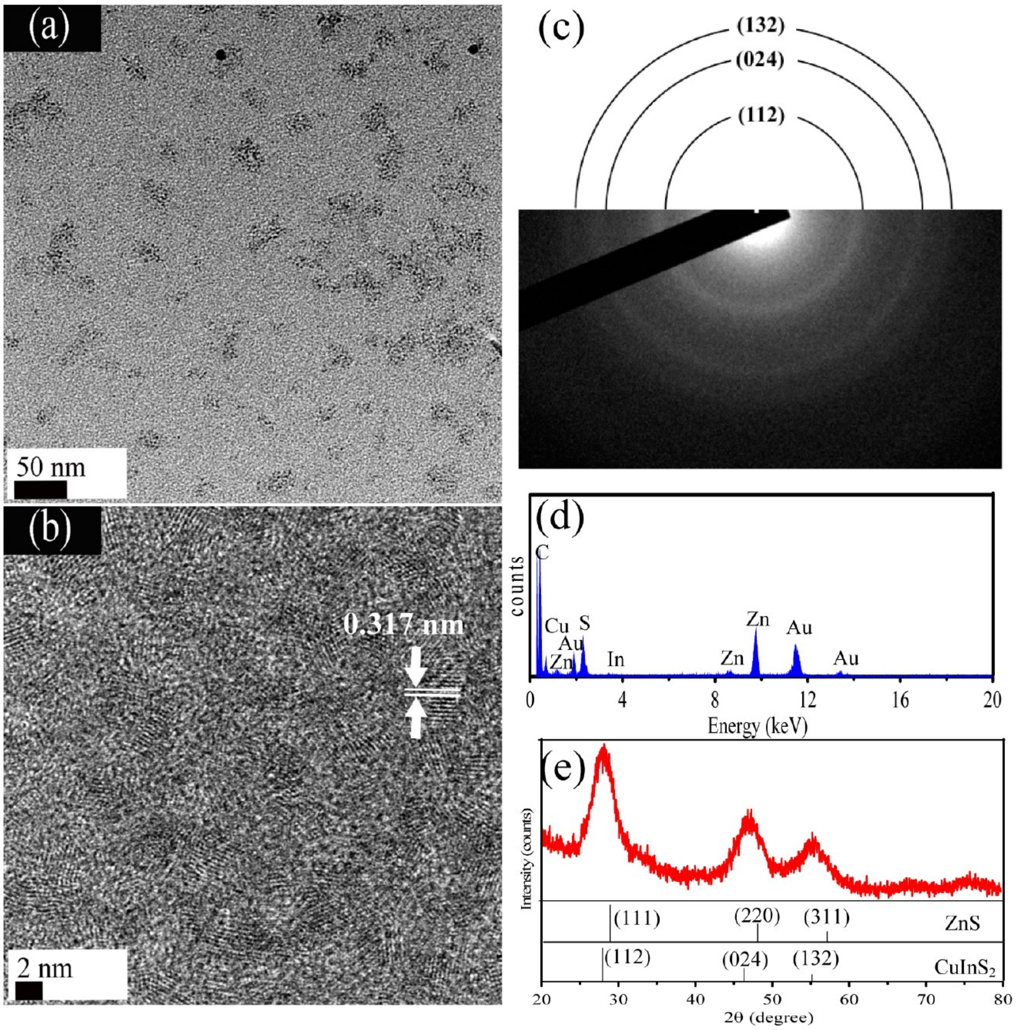

Figure 1. (a) Low-resolution and (b) high-resolution TEM images of CuInS2/ZnS QDs. (c) Selected area of electron diffraction pattern of CuInS2/ZnS QDs. (d) EDS spectra and (e) powder XRD patterns of the CuInS2/ZnS QDs. The XRD patterns of chalcopyrite CuInS2 (JCPDS 47−1372) and cubic zinc blende phase ZnS (JCPDS 80−0020) are also provided in d as a reference.

was stirred with magnetic stirring for about 60 min, and then the chloroform was removed by rotary evaporation. The remaining product was added to a clean glass vessel containing 0.5 mL of chloroform, followed by adding 3 mL (0.05 M) of NaOH. Subsequently, the solution was ultrasonicated for 1 min, and the chloroform was gradually removed under vacuum. The result was a clear, red colored solution of QD@PMO−COOH. The resulting solution was centrifuged at 20 000 rpm for 2 h to remove the excess PMO polymer. The supernatant was then discarded. The precipitate was redispersed in 13 mL of 0.02 M MES solution under sonication.

2.4. Preparation of Dual-Modality Nanoprobe (QD@PMO−Gd). Solutions (2 mL) of QD@PMO−COOH were synthesized as described above and followed by adding 6 mL of MES solution. The resulting solution was activated by adding 0.45 mmol EDC and 0.61 mmol NHS at room temperature for 30 min under conditions of moderate stirring. Subsequently, ethylenediamine (1.08 mmol) was added to the activated QD solution, and the mixture was stirred gently for 6 h at room temperature in the dark. The ethylenediamine-modified QD solution was further purified to remove excess ethylenediamine ligands and unreacted agents by tangential ultrafiltration with a poly(ethersulfone) membrane (MWCO 50 000 Da; Cellu. Sep H1, Orange Scientifique, Belgium). To conjugate the QDs with Gd(III)−DTPA, 0.45 mmol EDC and 0.61 mmol NHS were added to 2 mL of an MES solution containing 200 mg of Gd(III)−DTPA, and the mixture was stirred gently for 30 min. Afterward, the ethylenediamine-modified QD solution was added to the EDC/NHS activated Gd(III)−DTPA solution, followed by further stirring for another 24 h. The resulting solution was further purified to remove excess Gd(III)−DTPA ligands and unreacted agents by tangential ultrafiltration against 1 L of ultrapure water with a poly(ethersulfone) membrane (MWCO 50 000 Da; Cellu. Sep H1, Orange Scientifique, Belgium). The resulting solution was centrifuged at 20,000 rpm for 5 min. The supernatant was then discarded. The precipitate was redispersed in 8 mL of MES solution under sonication to obtain the purified dual-modality nanoprobe solution.

2.5. Preparation of Dual-Modality Nanoprobe Conjugated with Folic Acid (QD@PMO−Gd−FA). The dual-modality nanoprobe solution was activated with 0.23 mmol of EDC and 0.3 mmol of NHS in MES buffer (8.00 mL) with stirring at room temperature for 30 min, and then, 10 mL of folic acid (2.3 mM in MES) was slowly added into the above activated dual-modality nanoprobe solution while it was continuously stirred. After 24 h, the solution was centrifuged at 13 000 rpm for 5 min. The supernatant was then discarded. The precipitate was washed three times with MES solution to remove excess folic acid ligands and unreacted agents.

2.6. Cell Culture and Observation of Intracellular Location of QDs in Cancer Cells. Human cervical (HeLa), human liver carcinoma (HepG2), and human breast (MCF-7) cancer cells were cultured in Eagle's Minimum Essential Medium (containing 1.5 g/L sodium bicarbonate) supplemented with 1% L-glutamine, 1% antibiotic antimycotic formulation, 1% nonessential amino acid, 1% sodium pyruvate, and 10% fetal bovine serum. To induce cell expansion and

Scheme 1. Schematic Representation for the Synthesis of QD@PMO−COOH under the Assistance of Ultrasonication

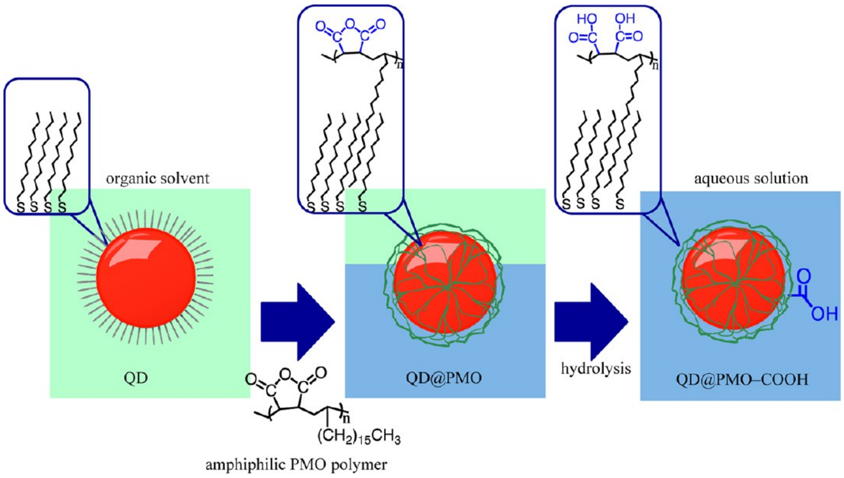

senescence, cells were cultured in a humidified 5% CO_2 atmosphere at 37 °C. Cells were seeded in a 6-well plate in 2 mL of culturing medium and cultured for 24 h before QDs were added. After 2 h of incubation with 300 μL of QDs, the cells were washed 3 times with phosphate-buffered saline (PBS) and then fixed with 75% alcohol for 10 min. Next, the fixed cells were incubated for 17 min at room temperature with 2 mL (0.05 μg/mL) DAPI in PBS for nucleus staining. The cells were washed twice with PBS and cell images were performed on the confocal laser scanning microscopy (Leica TCS SP2, 63 × 1.32 NA oil immersion objective, 488 nm Ar/Kr excitation wavelength).

2.7. In Vitro Cytotoxicity Measurement. The cytotoxicity of QDs was evaluated in various cells using an MTT assay. Briefly, cells were seeded in a 12-well plate at 5×10^4 cells per well. After 24 h to allow cell attachment, the cells were washed with PBS and incubated with 0, 2, 5, 10, 25, 50, and 100 μg/mL QDs for 24 h. The wells were then washed twice with PBS and 1 mL MTT reagent (500 μg mL^{-1}) was added to each well. The microplate was then reincubated at 37 °C in 5% CO_2 for 4 h, after which the medium was carefully aspirated. Subsequently, 200 μL of dimethyl sulfoxide was added to dissolve the dark-blue formazan crystals. The amount of dark-blue formazan crystals generated by the live cells was proportional to the number of live cells, and the absorbance at 570 nm was measured by using a Biotek Powerwave XS plate reader. All experiments were done in triplicate.

2.8. Characterization. High-resolution transmission electron microscopy (TEM) samples were prepared by dropping a dilute solution of QDs onto 3-mm gold grid covered with a continuous layer of carbon film. TEM imaging and energy dispersive X-ray spectroscopy (EDS) of QDs were performed on FEI Tecnai G2 F20 microscope (Philips, Holland), equipped with a field emission gun working at an accelerating voltage of 200 kV. Powder X-ray diffraction (XRD) patterns were collected using a Rigaku 18 kW rotating anode source X-ray diffractometer with the Cu $K_{\alpha 1}$ line (λ = 1.54 Å). The Fourier transform infrared (FTIR) spectra were measured with a Bio-Rad FTS-3500 spectrometer. KBr crystals were used as the matrix for sample preparation. UV−vis absorption spectra were measured with a JASCO V-630 spectrometer. Inductively coupled plasma atomic emission spectrometry (ICP-AES) (JY 2000−2, Jobin Yvon Horiba) was used for Gd(III) concentrations analysis. The measurements of PL spectra were carried out by using a JASCO FP-6500 spectrofluorometer equipped with a 150 W xenon lamp. The PL quantum yields (QY) of various samples were comparatively studied by taking rhodamine 6G (R6G) as a reference fluorescent dye with the known QY (95%) and comparing the integrated fluorescence intensity of the solutions, both recorded exciting samples having the same absorbance (<0.1 au in order to minimize possible reabsorption effects). The PL QYs of the as-prepared QDs were calculated using the following equations: $QY = QY_{R6G} I_{QD}/I_{R6G}(\eta_{chloroform}/\eta_{ethanol})$, where I and η denote the integral PL intensity and the optical density and reflective index of the solvent, respectively. Time-resolved single photon counting was performed with a PicoQuant PDL 200-B pulsed diode laser at a wavelength of 450 nm. The time-resolved decay curves were analyzed using the FluoFit software (PicoQuant, Germany) to extract lifetime values. The quality of the curve fitting was evaluated by reduced chi-square (χ^2). The T_1 relaxivity and MR images were obtained on a 7 T BioSpec 70/30 experimental scanner (70/30 Bruker BioSpin; Ettlingen, Germany) equipped with actively shielded gradient coils.

3. RESULTS AND DISCUSSION

$CuInS_2/ZnS$ QDs were prepared following our previous protocols[29] by using 1-dodecanethiol, containing long hydrocarbon tails as a hydrophobic protective agent and ODE as solvent. ODE is a low-cost, low-hazard, and air-stable liquid at room temperature, which boils at about 320 °C. During heat treatment, monomers accumulate in the ODE solution and burst nucleation occurs to generate seeds above the critical concentration. To improve the PL efficiency, ZnS material, having a wide direct bandgap to confine both electrons and holes in the QD core, was used as an inorganic shell for surface passivation of the $CuInS_2$ QDs. Images a and b in Figure 1 show representative low-resolution and high-resolution TEM images of $CuInS_2/ZnS$ QDs. The high-resolution TEM image of the $CuInS_2/ZnS$ QDs in Figure 1b displays clear lattice planes and good crystallinity with diameters of ∼2.5 nm. Figure 1c shows the corresponding electron diffraction pattern of indexed showing rings that are consistent with the [1,1,2], [0,2,4], and [1,3,2] reflections for chalcopyrite $CuInS_2$. The EDS spectra in Figure 1d indicate that the sample is composed of copper, indium, sulfur, and zinc. Figure 1e shows the XRD pattern of the $CuInS_2/ZnS$ QD consisting of three major peaks at 2θ values of 28.2, 46.9, and 55.2°, which were located between peaks associated with the chalcopyrite $CuInS_2$ and ZnS phases. Compared with the standard diffraction data of chalcopyrite $CuInS_2$ (JCPDS card no. 47−1372), the three major peaks are observed to shift to higher 2θ values, suggesting that the crystal structure of the $CuInS_2$ QD was slightly altered by Zn diffusion upon the preparation of the ZnS shell coating, causing a decrease in the lattice constant. These peaks are relatively broad, indicative of small crystalline particles in the as-prepared $CuInS_2/ZnS$ QDs. The size of QDs was estimated using the Debye−Scherrer equation[30]

$$D = K\lambda/\beta\cos(\theta)$$

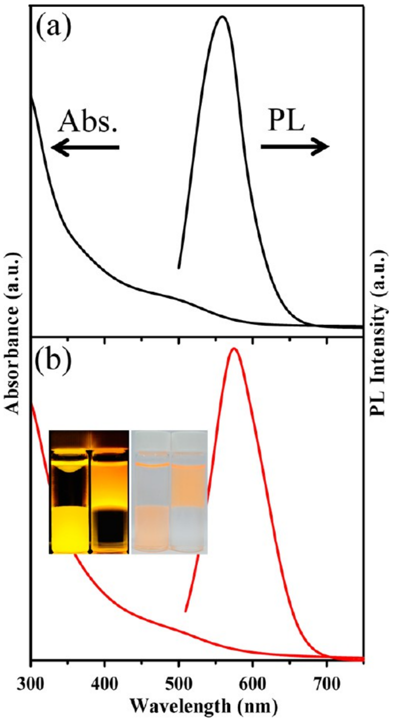

Figure 2. Normalized UV−vis absorption and PL (λ_{ex} = 430 nm) spectra of (a) a pristine $CuInS_2$/ZnS QD sample and (b) a QD@PMO−COOH sample. The four panel photographs in the inset show the QDs in chloroform (bottom two panels) before encapsulation and in water (top two panels) after being encapsulated with amphiphilic PMO polymer under irradiation with 365 nm ultraviolet light from a UV lamp (left two panels); the right two panels of the inset image show the corresponding samples observed under ambient light.

Scheme 2. Schematic Representation for the Synthesis of QD@PMO−Gd−FA Dual-Modality Nanoprobe

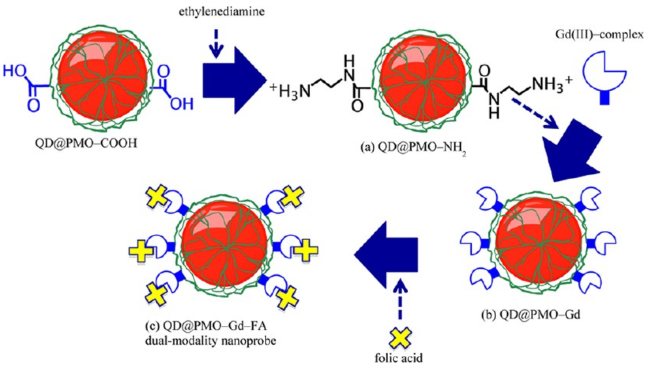

where D is the average crystallite size; λ is the X-ray wavelength; β is the width of a Bragg reflection in radians; and θ is the diffraction angle.

We estimated the average size of the QDs to be 3.2 nm from the (112) diffraction peak width (K the numerical constant was taken to be 0.9 assuming that the particles are spherical in shape), which is close to the average particle sizes determined by TEM measurements.

Hydrophilic $CuInS_2$/ZnS QDs were prepared by wrapping the surface capping agent with amphiphilic PMO polymers according to a previously modified report.[26,31−33] The strategy begins with the dispersion of $CuInS_2$/ZnS QDs and amphiphilic PMO polymers in the mixture solvent with the assistance of ultrasonication, as illustrated in Scheme 1. The coating procedure was based on self-organized wrapping of polymer around the QDs,[34] which indicated that hydrophobic aliphatic side chains of the amphiphilic PMO polymer form an interdigitated bilayer with hydrophobic protective agents (1-dodecanethiol) of the $CuInS_2$/ZnS QDs through hydrophobic van der Waals interactions. The maleic anhydride moieties of the amphiphilic PMO polymer that are exposed to the outermost part of the QDs can be readily hydrolyzed in water via ring-opening to form two carboxylate groups for each repeating unit across the polymer backbone. Thus, this wrapping process not only makes the QDs water-dispersible but also provides useful reactive groups for further functionalization.[32] This nanoarchitecture is referred to as QD@PMO−COOH. Figure 2 displays the absorbance and emission spectra of pristine QDs dissolved in chloroform as well as QD@PMO−COOH nanoprobes dissolved in water. The inset in Figure 2b shows four panels of photographic images of $CuInS_2$/ZnS QD samples coated with the original ligands (1-dodecanethiol) in chloroform (bottom two panels) and QD@PMO−COOH nanoprobe samples in water (top two panels) under UV irradiation (left two panels) and ambient light (right two panels). The intensities of the absorption and emission peaks were normalized. The wavelength of the maximum PL emission position (PL λ_{max}) of pristine QDs is around 560 nm. Compared with that of pristine QDs (Figure 2a), the peak shape of the QD@PMO−COOH nanoprobes did not change, but a red shift in the PL peak position and a small change in the full width at half-maximum values of the emission peak were observed.[35]

To introduce amine ligands, we activated the carboxyl groups of the QD@PMO−COOH nanoprobes with EDC, forming a reactive intermediate that includes an acylisourea ester, and this unstable species directly reacts with NHS resulting in the formation of a succinimidyl intermediate. This intermediate readily undergoes nucleophilic substitution with ethylenediamine, introducing the amine ligands on the PMO-coated QDs (denoted as QD@PMO−NH_2), as illustrated in Scheme 2a. After purification by dialysis, the QD@PMO−NH_2 nanoprobes were isolated and a fluorescamine test[36−38] was performed to prove the presence of primary amines on the nanoprobe. Fluorescamine intrinsically has no fluorescence, but it becomes fluorescent through reaction with primary amines. Figure 3a shows that the emission peak position of the tested QD@PMO−NH_2 nanoprobe sample is 580 nm upon irradiation with a 390 nm light source. The spectrum of the QD@PMO−NH_2 nanoprobe sample treated with fluorescamine exhibits an additional emission band centered at 475 nm apart from the intrinsic emission of the QDs at 580 nm, which corresponds to the presence of a significant number of primary amines on the nanoprobe surface.

T_1-weighted MR agents offer favorably brighter/positive contrast enhancement for both vascular imaging and tumor imaging, and generally provide images of higher resolution and signal-to-noise ratio than T_2-weighted agents. Of the different T_1-weighted MR agents, Gd(III)-chelates such as Gd(III)−DTPA have been widely used because of their contrast enhancement and high stability in vivo.[39,40] However, the intrinsically low molecular weight of Gd(III)−DTPA results in short blood circulation times because of rapid excretion through urine, which hampers high-resolution imaging requiring extended scanning times. In this study, the Gd(III)−DTPA MR agent was covalently attached to the surface

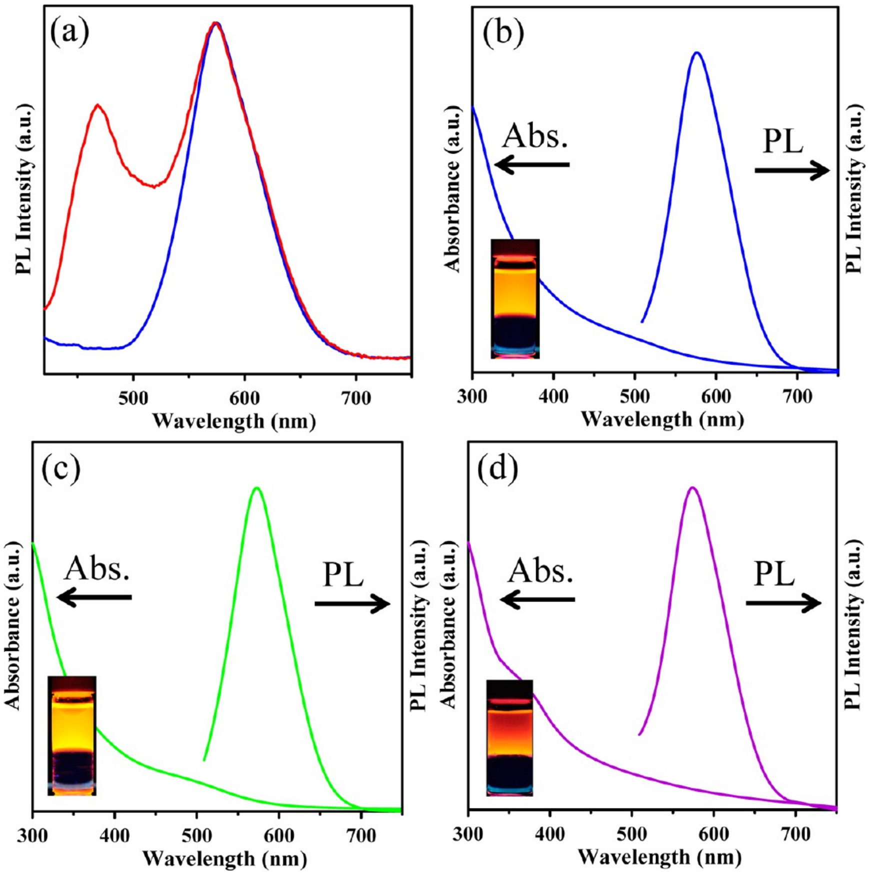

Figure 3. (a) Normalized PL (λ_{ex} = 390 nm) spectra of a QD@PMO−NH_2 nanoprobe sample before (blue line) and after (red line) examination with fluorescamine. Normalized UV−vis absorption and PL (λ_{ex} = 430 nm) spectra of (b) QD@PMO−NH_2, (c) QD@PMO−Gd, and (d) QD@PMO−Gd−FA nanoprobe samples. The insets provide two-panel photographs showing each corresponding nanoprobe in solution under irradiation with 365 nm ultraviolet light from a UV lamp. The top panel photographs are samples in water and bottom panels are samples in chloroform.

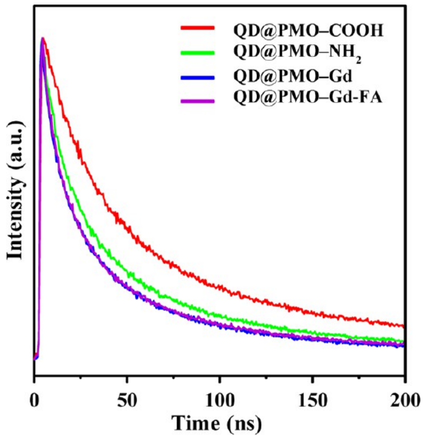

Figure 4. Time−resolved PL decay curves of the nanoprobe samples recorded at room temperature.

of the QD@PMO−NH_2 nanoprobe to integrate the discussed MR imaging capability while extending blood circulation times. A cross-linker reagent, EDC/NHS, was added again to construct the covalent attachment between the QD@PMO−NH_2 nanoprobe and carboxyl groups of Gd(III)−DTPA for the formation of the Gd(III)-complex on the nanoprobe surface. In this process, the carboxyl group of Gd(III)−DTPA is first activated with the EDC agent to generate a reactive and unstable *o*-acylisourea intermediate. This unstable intermediate subsequently reacts with the NHS agent causing a semistable amino-reactive NHS-ester in the Gd(III)-complex, which will react with available amines on the surface of the nanoprobe, forming a Gd(III)−DTPA−nanoprobe conjugate joined by a stable amide bond (denoted as QD@PMO−Gd in Scheme 2b). The QD@PMO−Gd nanoprobes bearing carboxyl groups could be conjugated with different molecules (e.g., antibodies, enzymes, or DNA/RNA through hybridization). Although many antibodies or specific ligands can selectively bind to the

Table 1. Fluorescence Lifetime Parameters for Different Samples[a]

sample	τ_1 (ns)	A_1(%)	τ_2 (ns)	A_2(%)	τ_{av} (ns)	χ^2
QD@PMO−COOH	208.2	37.10	49.17	62.90	162.8	1.08
QD@PMO−NH_2	186.0	33.26	45.17	66.74	139.8	1.04
QD@PMO−Gd	172.7	31.75	43.70	68.25	127.3	1.09
QD@PMO−Gd−FA	172.7	29.78	41.95	70.22	125.1	1.07

[a] λ_{ex} = 450 nm, λ_{em} ≈ peak maximum.

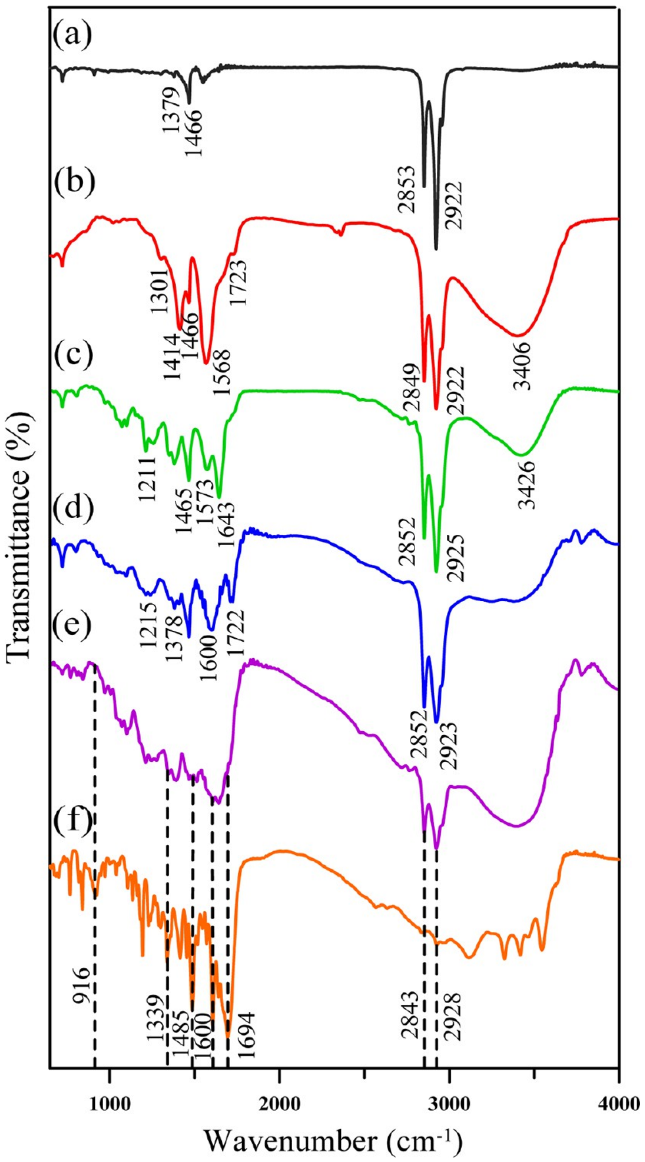

Figure 5. FTIR spectra of (a) pristine $CuInS_2$/ZnS QDs, (b) QD@PMO−COOH, (c) QD@PMO−NH_2, (d) QD@PMO−Gd, (e) QD@PMO−Gd−FA, and (f) neat folic acid.

cells, folic acid is a promising candidate for cancer-cell targeting. To demonstrate the targeting capability of these synthesized QD@PMO−Gd nanoprobes, we used folic acid as a target ligand instead of another specific antibody for the following reasons. It is well-known that folic acid, which is a glycosylphosphatidyl-inositol-anchored (GPI-anchored) membrane glycoprotein, has high affinity for the folate receptor ($K_d \approx 1 \times 10^{-10}$ M). Folic acid acts as a cancer-cell-targeting ligand because the folate receptor is overexpressed in many human cancerous cells, including ovarian cancer and squamous cell carcinoma, but rarely distributed in normal cells.[41] Moreover, because of its high stability, low cost, low molecular mass (38−40 kDa), nonimmunogenic character, and capability of being conjugated with various organic molecules, nanoparticles, or polymers, folic acid is a particularly promising targeting agent.[42−45] Therefore, the QD@PMO−Gd nanoprobe was further conjugated with folic acid by adopting a carbodiimide chemistry. In this experiment, the QD@PMO−Gd nanoprobe was activated with EDC/NHS, which mediated cross-coupling between the amino and carboxyl groups on the folic acid and nanoprobe, respectively (denoted as QD@PMO−Gd−FA in Scheme 2c).

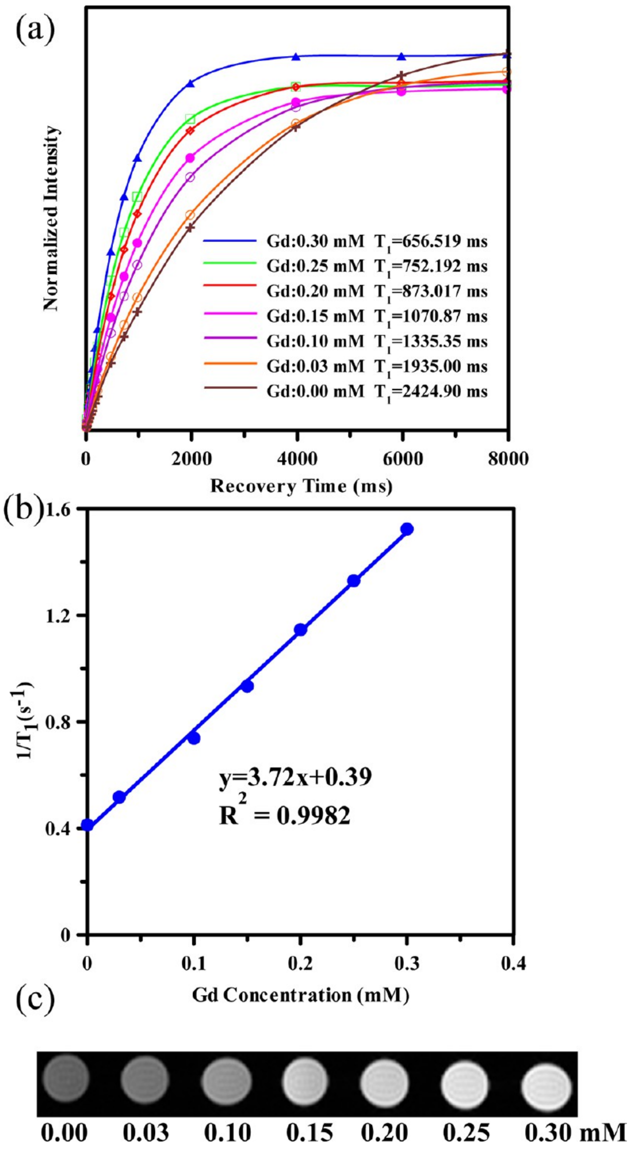

Figure 6. (a) MR signal intensities of the QD@PMO−Gd−FA nanoprobe material in aqueous solution for different values of Gd(III) concentration (mM) as a function of recovery time. The symbols and solid lines are the experimental data and the results of fitting the experimental data to the exponential curve given in the main text, respectively. (b) T_1 relaxation rates ($1/T_1$, s^{-1}) of the QD@PMO−Gd−FA nanoprobe material in aqueous solution as a function of Gd(III) concentration (mM). (c) T_1-weighted MR images of QD@PMO−Gd−FA aqueous solutions with different Gd(III) concentrations. Deionized water (0 mg mL^{-1}) served as the reference.

The optical properties of QD@PMO−NH_2, QD@PMO−Gd, and QD@PMO−Gd−FA nanoprobes were examined by UV−vis absorbance and PL spectroscopy, and the results presented in Figure 3b−d. The intensities of the absorption and emission peaks were normalized. The PL λ_{max} of the QD@PMO−NH_2, QD@PMO−Gd, and QD@PMO−Gd−FA nanoprobes is around 573, 576, and 574 nm, respectively. Using R6G as a standard, the PL QYs of these nanoprobes was calculated to be around 1% in aqueous solution. All aqueous nanoprobe dispersions exhibited similar emission profiles, and

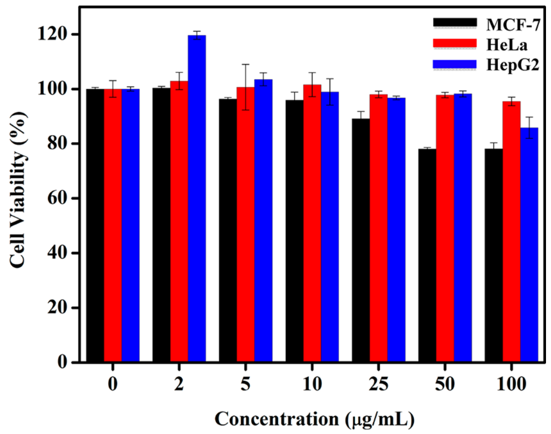

Figure 7. In vitro cell viability of HeLa, HepG2, and MCF-7 cells incubated with QD@PMO−Gd−FA for 24 h at 37 °C as a function of different nanoprobe concentrations: 0 (as a control), 2, 5, 10, 25, 50, and 100 μg/mL. Deionized water (0 μg/mL) served as the control.

were nearly identical to that of the QD@PMO−COOH nanoprobe. These results suggest that there are no apparent effects on the electronic and optical properties of $CuInS_2/ZnS$ QDs upon conjugation reaction with different ligands (e.g., ethylendiamine, Gd(III)−DTPA, and folic acid). Moreover, the colloidal stability of QD@PMO−Gd−FA nanoprobes was tested over a range of pH. Figure S1a in the Supporting Information showed the fluorescence of several solutions of red-emitting QD@PMO−Gd−FA nanoprobes, which dispersed in 2 mL of 20 mM MES solution over a pH range of 5−12. The result indicated that no visible sign of aggregation in the pH range of 6−8 after 72 h storage. The QD@PMO−Gd−FA dispersions also showed luminescent colloidal stability in pH 7 solutions with different ionic strengths (from 0 to 0.5 M NaCl) after storing for 72 h (see Figure S1b in the Supporting Information).

Most organic fluorophores have their lifetimes in a range of several nanoseconds, close to the lifetime of cellular autofluorescence, and as a result, the emission signals from them cannot be well resolved from the cellular backgrounds in

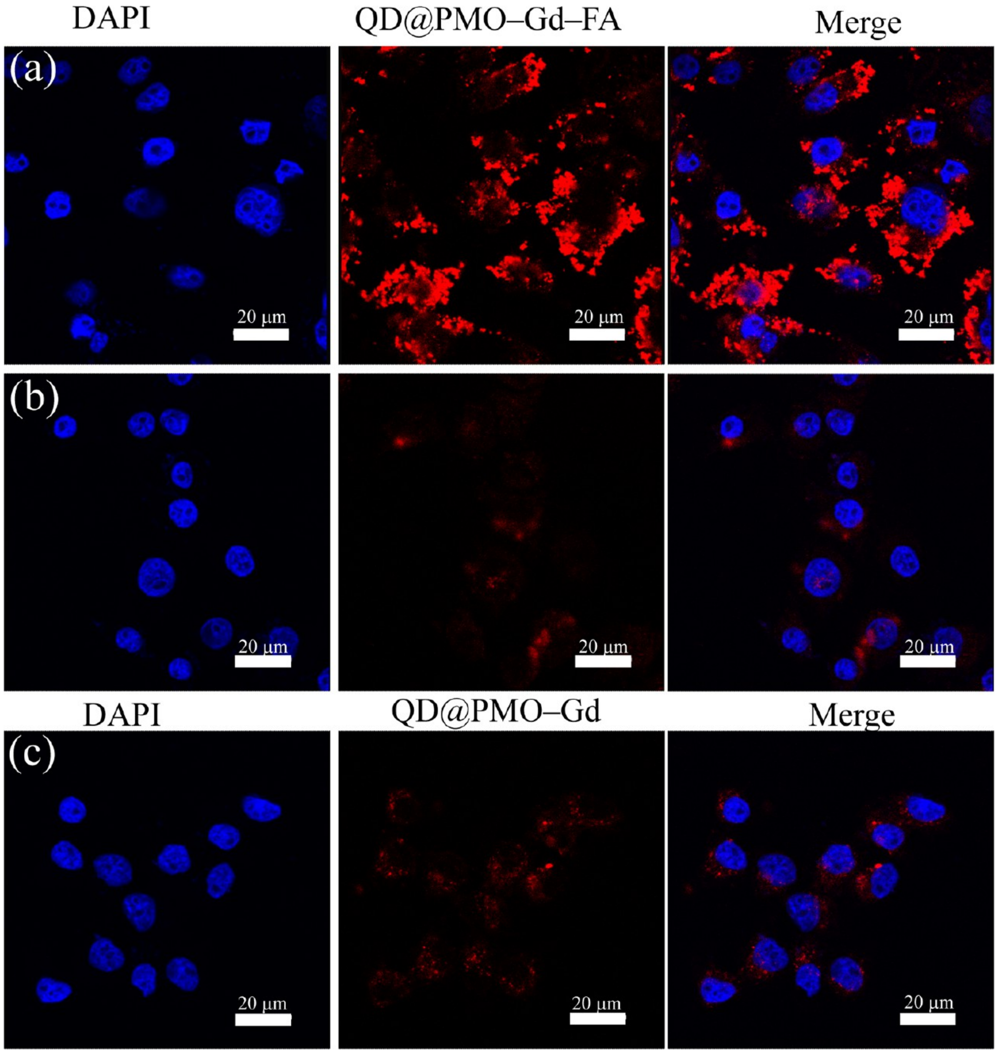

Figure 8. (a, b) Confocal laser scanning fluorescent microscopy images of HeLa cells incubated with a 100 μg/mL solution of QD@PMO−Gd−FA, and subsequently fixed with alcohol and stained with DAPI. In b, the cells were subjected to competition study by concurrently incubating the cells with 10 mM of free excess folic acid for 1 h with the QD nanoprobe solution. (c) Cells treated with a 100 μg/mL solution of QD@PMO−Gd for 1 h and again stained with DAPI. In all cases, blue fluorescence shows DAPI-stained nuclei and red fluorescence represents localization of QD nanoprobes.

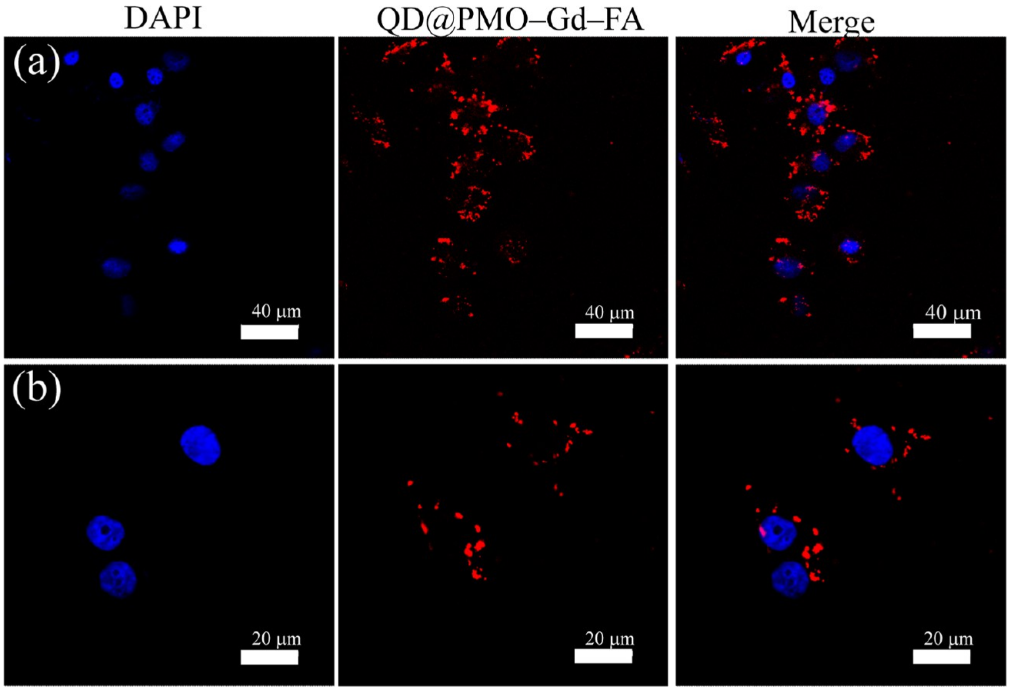

Figure 9. Confocal laser scanning fluorescence microscopy images showing fluorescence of (a) HepG2 and (b) MCF-7 cancer cells after 1 h of incubation with a 100 μg/mL solution of QD@PMO−Gd−FA, as well as subsequently being fixed with alcohol and stained with DAPI. In all cases, blue fluorescence shows DAPI-stained nuclei and red fluorescence represents localization of QD nanoprobes.

lifetime cell imaging.[46,47] Long PL lifetime is also crucial for constructing simple and low-cost instruments for time-resolved confocal measurement. To better understand the fluorescence mechanism, the time-resolved PL decay of the nanoprobes at different conditions was studied. Figure 4 shows the PL decay curves of QD@PMO−COOH, QD@PMO−NH_2, QD@PMO−Gd, and QD@PMO−Gd−FA nanoprobes. The PL decay profiles of all the samples were fitted in terms of biexponential decay profile ($I(t) = A_1 \exp(-t/\tau_1) + A_2 \exp(-t/\tau_2)$), where $\tau_1$and τ_2 are the decay time of the PL emission as well as A_1 and A_2 are the relative weights of the decay components at $t = 0$). The average lifetimes τ_{av}, determined by the expression $\tau_{av} = (A_1\tau_1^2 + A_2\tau_2^2)/(A_1\tau_1 + A_2\tau_2)$ are also summarized in Table 1. The PL decay lifetime of $CuInS_2$/ZnS QDs upon conjugation reaction with different ligands showed very similar luminescence decay kinetics with radiative lifetimes of 140 ± 20 ns. It is clear from our observation that the lifetime of the dual-modality nanoprobes in this study are significantly longer than most organic fluorophores or II−VI QDs. Their long lifetimes make them particularly appealing for the visualization of cellular processes in time-resolved confocal measurements, which can eliminate unwanted interfering background for high-sensitivity assays.

Fourier transform infrared spectroscopy (FTIR) studies were employed to verify the structural characteristics of pristine $CuInS_2$/ZnS QD, QD@PMO−COOH, QD@PMO−NH_2, QD@PMO−Gd, and QD@PMO−Gd−FA nanoprobes, as shown in Figure 5. In the FTIR spectrum of the pristine $CuInS_2$/ZnS QDs coated with 1-dodecanthiol (Figure 5a), the strong doublet observed at 2853 and 2922 cm^{-1} can be assigned to the symmetric and asymmetric $-CH_2$ stretching vibrations of the alkyl hydrocarbon, whereas methyl symmetric rocking is attributable to the spectrum located between 1390−1370 cm^{-1}, and methyl asymmetric rocking/CH_2 scissoring is indicated by the spectrum at 1466 cm^{-1}. In the case of QD@PMO−COOH nanoprobe (Figure 5b), the broad absorption band at 3406 cm^{-1} can be attributed to the OH group, and the bands appearing at 2922 (or 2849), 1466, and 1414 cm^{-1} correspond to C−H stretching, C−H bending, and C−O stretching vibrations, respectively. Moreover, the stretching of the C═O bond observed at 1568 cm^{-1} is consistent with the presence of a carboxylic acid group. Upon introducing amine groups on the surface of the QDs (i.e., in the case of QD@PMO−NH_2 nanoprobe), in Figure 5c, we observe a corresponding appearance of an absorption band at 1643 cm^{-1} assigned to the amide carbonyl (C═O) stretch. Two characteristic bands at 2925 and 2852 cm^{-1} were attributed to aliphatic C−H stretching modes. The bands at 1573, 1465, and 1121 cm^{-1} are assigned to N−H in-plane bending, C−H bending, and C−N stretching modes, respectively. In addition, the broadband between 3300−3500 cm^{-1} can be assigned to $-NH_2$ stretching. These results provide qualitative information about ethylenediamine molecules grafted onto the surface of the QDs forming QD@PMO−NH_2. After the attachment of Gd(III)−DTPA onto the surface of the nanoprobe, it was found that the absorption bands for the QD@PMAO−Gd nanoprobe, shown in Figure 5d at 2923 and 2852 cm^{-1}, were attributed to the C−H stretching vibrations. The bands observed at 1722, 1600, 1378, and 1215 cm^{-1} can be assigned to the C═O stretching vibration of the carboxyl group, C═C stretching vibration, O−H deformation and C−N stretching vibration, respectively. Following folic acid immobilization, it was found that most of the characteristic vibrational modes of folic acid (Figure 5f) also appear in the FTIR spectrum of the QD@PMO−Gd−FA nanoprobe (Figure 5e), such as C−H stretching at 2928 and 2843 cm^{-1}, aromatic ring stretching of the pteridine ring, and *p*-amino benzoic acid moieties of folic acid within the range 1476−1694 cm^{-1}.[48] The peaks located at 1339 and 916 cm^{-1} are also evidence of these moieties, corresponding to aromatic C−H in-plane and out-of-plane bending in folic acid. The increased intensity of the −OH stretching vibration frequency at 3200 cm^{-1} can also reflect the contribution of the folic acid molecules conjugated with the nanoprobe.

The MR imaging mechanisms are based on excitation and relaxation of hydrogen nuclei that are abundant in water and lipids of tissue. The intrinsic longitudinal (T_1) and transverse (T_2) relaxation times of different parts of biological tissue bring about changes in the MR signal intensity, which in turn results in an imaging contrast. To assess the effectiveness of dual-modality QD@PMO−Gd−FA nanoprobes as MR imaging contrast agents, the magnetic resonance relaxivity of the dual-modality QD@PMO−Gd−FA nanoprobe material was measured using a clinical MR scanner at room temperature. The Gd(III) concentration of the QD@PMO−Gd−FA nanoprobe in a solution was determined by ICP-AES, and solutions with different Gd(III) concentrations were thereby obtained by dilution with hyperpure water. The T_1 relaxation times for various Gd(III) concentrations were obtained by evaluating the MRI signal intensities at different recovery times and fitting the data to the following exponential function: $M(T_R) = M_0(1 - K\exp(-T_R/T_1))$, where $M(T_R)$ is the MR signal intensity at a recovery time T_R, M_0 is the MRI signal intensity at equilibrium or before inversion, and K is a constant related to the background noise. The set of recovery times, T_R, used for determination was 38.87, 50, 75, 100, 125, 150, 200, 250, 500, 750, 1000, 2000, 4000, 6000, and 8000 ms. The resulting experimental measurements and fitted curves are given in Figure 6a. Figure 6b shows the graph of the longitudinal relaxation rates ($1/T_1$) plotted against the Gd(III) concentration for dual-modality QD@PMO−Gd−FA nanoprobe solutions. The relaxation rates exhibit a linear relationship with respect to the Gd(III) concentration. The longitudinal relaxivity (r_1) value (determined by the slope of a linear fit of the plot of $1/T_1$ versus Gd(III) concentration) is 3.72 mM^{-1} s^{-1} for the as-prepared QD@PMO−Gd−FA nanoprobe solution. In Figure 6c, we can observe a clear, positive, and increasing contrast enhancement of MR signals occurring concurrently with a gradually increasing Gd(III) concentration. This indicates that the Gd(III)-complex on the surface of the QD@PMO−Gd−FA nanoprobe enhances the longitudinal proton relaxation process, and thus, QD@PMO−Gd−FA nanoprobe solutions could be employed as effective T_1 contrast agents. For a comparison, QD@PMO and QD@PMO−FA nanoprobes in the absence of Gd(III)-complex linker molecules were designed as a control experiment (see Figure S2 in the Supporting Information). Typically, contrast agents are administered to enhance the signal effects and produce a clear and sensitive image. However, the result show similar corresponding signal intensity as compared with the signal intensity of deionized water, which indicates that the sole presence of $CuInS_2$/ZnS QDs cannot reduce or increase the longitudinal relaxation time of water protons.

To verify the potential application of the QD@PMO−Gd−FA nanoprobe as a bioprobe in bioimaging, it is necessary to evaluate its in vitro cytotoxicity. To this end, an MTT assay was performed on HeLa, MCF-7, and HepG2 cells, as shown in Figure 7. In the MTT assay, the optical absorbance of formazan (produced by the cleavage of MTT by dehydrogenases in living cells) at a wavelength of 570 nm, as measured by spectrophotometer, is directly proportional to the number of live cells.[49] The concentration-dependent effect of the QD@PMO−Gd−FA nanoprobe on the HeLa cell viability after 24 h was determined. It was demonstrated that, after 24 h of incubation, more than 90% of the HeLa cells survived, even at a high QD@PMO−Gd−FA nanoprobe concentration (100 μg/mL). In addition, it can be seen from Figure 7 that the QD@PMO−Gd−FA nanoprobe showed no significant cytotoxic effect on both HepG2 and MCF7 cells, in the concentration range of 2−100 μg/mL after incubation for 24 h. Even with a concentration as high as 100 μg/mL, the HepG2 and MCF7 cell viability remained at about 80%. On the basis of the above-mentioned MTT results, it can be deduced that the QD@PMO−Gd−FA nanoprobe is highly biocompatible and non-toxic to living cells. From this standpoint, such a low level of in vitro cytotoxicity implies that the QD@PMO−Gd−FA nanoprobe can serve as an intracellular marker for diagnosis.

HeLa cells were incubated with a 100 μg/mL QD@PMO−Gd−FA nanoprobe solution for 1 h, and the cells were washed to remove any noninternalized nanoprobe. The cells were then subjected to confocal laser scanning fluorescent microscopy. The confocal microscope images are shown in Figure 8. An intense red fluorescence originated from the emission of the QD@PMO−Gd−FA nanoprobe, which was observed to be distributed throughout the cytoplasm region of the cell in the middle micrograph of Figure 8a. To visualize the cell nuclei, we also stained the cells with DAPI, a nuclear staining dye known to reveal an intense blue PL when bound to DNA, as observed in the left-side micrograph of Figure 8a. Consideration of the merged images in the right-side micrograph of Figure 8a indicates that the observed red luminescence is distributed in almost all cells throughout the entire cell cytoplasm. This suggests that QD@PMO−Gd−FA nanoprobes are distributed throughout the cells. QD@PMO−Gd−FA nanoprobes are expected to be efficiently bound to or delivered into HeLa cells due to folate-receptor-mediated endocytosis. To verify that the uptake of QD@PMO−Gd−FA nanoprobes into cells can be mainly driven by folate-receptor-mediated endocytosis, we also performed competition experiments under the same experimental conditions described above by conducting QD@PMO−Gd−FA nanoprobe incubation in the presence of 10 mM free excess folic acid simultaneously. As a result, as shown in Figure 8b, the uptake of QD@PMO−Gd−FA nanoprobes by HeLa cells was significantly reduced in the presence of free folic acid and negligible fluorescence was detected. It can be reasonably assumed that the observed reduction is because excess free folic acid partially binds to the surface receptors of HeLa cancer cells and thus inhibits intracellular uptake of the nanoprobe. The results shown in Figure 8b strongly suggests that QD@PMO−Gd−FA nanoprobe uptake is associated with folate-receptor-mediated targeted delivery. As an additional control, HeLa cells were also incubated for 1 h with a 100 μg/mL solution of QD@PMO−Gd nanoprobes, which therefore did not carry folic acid molecules at their surface. As can be observed in Figures 8c, the QDs@PMO−Gd nanoprobes showed little internalization in Hela cells after 1 h of incubation. However, the results indicate that the QD@PMO−Gd nanoprobes without folic acid moieties can still be ingested by HeLa cells, indicating that a nonreceptor-mediated endocytosis pathway exists in HeLa cells. This result is also consistent with previous reports,[50] in which silicon/iron oxide hybrid nanoparticles were well internalized by HeLa cells even without folic acid modification on the surface. Such passive targeting without any receptor modification takes place frequently in HeLa cells (*e.g.*, silicon QDs,[51] graphene-based probes,[47,48,52,53] Gd-enriched DNA−Au nanoparticles,[54] and

CdSe/CdZnS QDs[55]). In contrast, the liver hepatocellular carcinoma HepG2 and nonaggressive breast carcinoma MCF-7 cells are both folate receptor deficient cancer cell lines. The above two cell lines were further employed to evaluate cell selectivity characteristics of the QD@PMO−Gd−FA. Images a and b in Figure 9 show HepG2 and MCF-7 cells subjected to an identical incubation and staining procedure as conducted for HeLa cells and examined by confocal fluorescence microscopy. Figure 9 demonstrates that HepG2 and MCF-7 cells rarely internalized the QD@PMO−Gd−FA nanoprobes, and only punctuated red fluorescence is seen to be dispersed throughout the cytoplasm, compared with that observed for HeLa cells in Figure 8a under the same incubation conditions. It is reasonable to deduce then that because HepG2 and MCF-7 cells rarely possess folate receptors on their membrane surface, they are incapable of internalizing significant amounts of the QD@PMO−Gd−FA nanoprobe solution. For comparison, control experiments performed with QD@PMO nanoprobes resulted in no noticeable intracellular QD fluorescence in HeLa, HepG2, and MCF-7 cells (see Figure S3 in the Supporting Information).

4. CONCLUSIONS

Herein, we demonstrate for the first time not only the facile fabrication of Gd-based $CuInS_2$/ZnS nanoprobes with magnetic resonance/optical imaging capability, but also the grafting of a targeting agent (folic acid) on the surface of the nanoprobes. This dual-modality nanoprobe demonstrated good biocompatibility with respect to in vitro cytotoxicity tests conducted by MTT assay on HeLa, HepG2, and MCF-7 cells. MR imaging characterization revealed that the dual-modality nanoprobe elicits T_1 relaxivity ($r_1 = 3.7231$ $mM^{-1}s^{-1}$) and we can observe a clear, positive, and increasing contrast enhancement of magnetic resonance signals concurrently with an increasing Gd(III) concentration of QD@PMO−Gd−FA nanoprobes. Confocal scanning laser imaging characterization revealed that the QD@PMO−Gd−FA nanoprobes target HeLa cells most specifically and effectively via folate-receptor-mediated targeted delivery compared with HepG2 and MCF-7 cells, which would be beneficial for evaluating the stage of tumor progression and making treatment decisions. These results indicate that the QD@PMO−Gd−FA nanoprobe has the potential to be used as a platform for dual-modality imaging (both magnetic resonance and fluorescence) and specific targeting (via folate-receptor-mediated targeted delivery) in various biological systems. We expect that these results will open up a way to take advantage of the full potential of I−III−VI QDs for biological in vitro and in vivo studies.

■ ASSOCIATED CONTENT

Ⓢ Supporting Information

The colloidal stability test and the optical/MR images of control experiment. This material is available free of charge via the Internet at http://pubs.acs.org/.

■ AUTHOR INFORMATION

Corresponding Author

*E-mail: jychang@mail.ntust.edu.tw (J.-Y.C.); jasonyang@fusol-material.com (C.-H.Y.). Tel.: +886-2-27303636. Fax: +886-2-27376644.

Author Contributions

‡C.-Y. Cheng and K.-L. Ou contributed equally to this work

Notes

The authors declare no competing financial interest.

■ ACKNOWLEDGMENTS

The authors thank the National Science Council of the Republic of China for financially supporting this research under Contract NSC 101-2113-M-011-002, and supporting partly by Taipei Medical University under Contract TMU102-BIMDPP-02. We also thank the National Taiwan University of Science and Technology-Taipei Medical University Joint Research Program for financially supporting this research under Contract TMU-NTUST-101-06. We thank 7T animal MRI Core Lab of the Neurobiology and Cognitive Science Center, National Taiwan University, for technical and facility supports.

■ REFERENCES

(1) Liu, Y.; Zhang, N. *Biomaterials* **2012**, *33*, 5363−5375.
(2) Hu, F.; Joshi, H. M.; Dravid, V. P.; Meade, T. J. *Nanoscale* **2010**, *2*, 1884−1891.
(3) Qin, J.; Laurent, S.; Jo, Y. S.; Roch, A.; Mikhaylova, M.; Bhujwalla, Z. M.; Muller, R. N.; Muhammed, M. *Adv. Mater.* **2007**, *19*, 1874−1878.
(4) Liu, T.; Li, X.; Qian, Y.; Hu, X.; Liu, S. *Biomaterials* **2012**, *33*, 2521−2531.
(5) Na, H. B.; Hyeon, T. *J. Mater. Chem.* **2009**, *19*, 6267−6273.
(6) Bakalova, R.; Zhelev, Z.; Aoki, I.; Masamoto, K.; Mileva, M.; Obata, T.; Higuchi, M.; Gadjeva, V.; Kanno, I. *Bioconjugate Chem.* **2008**, *19*, 1135−1142.
(7) Yang, H.; Santra, S.; Walter, G. A.; Holloway, P. H. *Adv. Mater.* **2006**, *18*, 2890−2894.
(8) Oostendorp, M.; Douma, K.; Hackeng, T. M.; Post, M. J.; van Zandvoort, M. A. M. J.; Backes, W. H. *Magn. Reson. Med.* **2010**, *64*, 291−298.
(9) Diagaradjane, P.; Deorukhkar, A.; Gelovani, J. G.; Maru, D. M.; Krishnan, S. *ACS Nano* **2010**, *4*, 4131−4141.
(10) Koole, R.; van Schooneveld, M. M.; Hilhorst, J.; Castermans, K.; Cormode, D. P.; Strijkers, G. J.; Donega, C. M.; Vanmaekelbergh, D.; Griffioen, A. W.; Nicolay, K.; Fayad, Z. A.; Meijerink, A.; Mulder, W. J. M. *Bioconjugate Chem.* **2008**, *19*, 2471−2479.
(11) Prinzen, L.; Miserus, R.-J. J. H. M.; Dirksen, A.; Hackeng, T. M.; Deckers, N.; Bitsch, N. J.; Megens, R. T. A.; Douma, K.; Heemskerk, J. W.; Kooi, M. E.; Frederik, P. M.; Slaaf, D. W.; van Zandvoort, M. A. J.; Reutelingsperger, C. P M. *Nano Lett.* **2007**, *7*, 93−100.
(12) Park, J.; Bhuniya, S.; Lee, H.; Noh, Y. -W.; Lim, Y. T.; Jung, J. H.; Hong, K. S.; Kim, J. S. *Chem. Commun.* **2012**, *48*, 3218−3220.
(13) Mulder, W. J.; Koole, R.; Brandwijk, R. J.; Storm, G.; Chin, P. T. K.; Strijkers, G. J.; Donega, C. M.; Nicolay, K.; Griffioen, A. W. *Nano Lett.* **2006**, *6*, 1−6.
(14) Liu, L.; Law, W. -C.; Yong, K. -T.; Roy, I.; Ding, H.; Erogbogbo, F.; Zhang, X.; Prasad, P. N. *Analyst* **2011**, *136*, 1881−1886.
(15) Li, L.; Daou, T. J.; Texier, I.; Chi, T. T. K.; Liem, N. Q.; Reiss, P. *Chem. Mater.* **2009**, *21*, 2422−2429.
(16) Pons, T.; Pic, E.; Lequeux, N.; Cassette, E.; Bezdentnaya, L.; Guillemin, F.; Marchal, F.; Dubertret, B. *ACS Nano* **2010**, *4*, 2531−2538.
(17) Li, L.; Pandey, A.; Werder, D. J.; Khanal, B. P.; Pietryga, J. M.; Klimov, V. I. *J. Am. Chem. Soc.* **2011**, *133*, 1176−1179.
(18) Xie, R.; Rutherford, M.; Peng, X. *J. Am. Chem. Soc.* **2009**, *131*, 5691−5697.
(19) Chen, B.; Zhong, H.; Zhang, W.; Tan, Z.; Li, Y.; Yu, C.; Zhai, T.; Bando, Y.; Yang, S.; Zou, B. *Adv. Funct. Mater.* **2012**, *22*, 2081−2088.
(20) Deng, D.; Chen, Y.; Cao, J.; Tian, J.; Qian, Z.; Achilefu, S.; Gu, Y. *Chem. Mater.* **2012**, *24*, 3029−3037.
(21) Palmer, T. N.; Caride, V. J.; Caldecourt, M. A.; Twickler, J.; Abdullah, V. *Biochim. Biophys. Acta* **1984**, *797*, 363−368.

(22) Maeda, H.; Wu, J.; Sawa, T.; Matsumura, Y.; Hori, K. *J. Controlled Release* **2000**, *65*, 271−284.
(23) Cassette, E.; Pons, T.; Bouet, C.; Helle, M.; Bezdetnaya, L.; Marchal, F.; Dubertret, B. *Chem. Mater.* **2010**, *22*, 6117−6124.
(24) Wang, M.; Liu, X.; Cao, C.; Wang, L. *J. Mater. Chem.* **2012**, *22*, 21979−21986.
(25) Subramaniam, P.; Lee, S. J.; Shah, S.; Patel, S.; Starovoytov, V.; Lee, K. -B. *Adv. Mater.* **2012**, *24*, 4014−4019.
(26) Chang, J. -Y.; Wnag, G. Q.; Cheng, C. -Y.; Lin, W. -X.; Hsu, J. -C. *J. Mater. Chem.* **2012**, *22*, 10609−10618.
(27) Park, J.; Dvoracek, C.; Lee, K. H.; Galloway, J. F.; Bhang, H. C.; Pomper, M. G.; Searson, P. C. *Small* **2011**, *7*, 3148−3152.
(28) Fahmi, M. Z.; Chang, J. -Y. *Nanoscale* **2013**, *5*, 1517−1528.
(29) Hsu, J. -C.; Huang, C. -C.; Qu, K. -L.; Lu, N.; Mai, F. -D.; Chen, J. -K.; Chang, J. -Y. *J. Mater. Chem.* **2011**, *21*, 19257−19266.
(30) Compagnini, G.; Fragala, M. E.; D'Urso, L.; Spinella, C.; Puglisi, O. *J. Mater. Res.* **2001**, *16*, 2934−2938.
(31) Moros, M.; Hernaez, B.; Garet, E.; Dias, J. T.; Saez, B.; Grazu, V.; Gonzalez-Fernandez, A.; Alonso, C.; de la Fuente, J. M. *ACS Nano* **2012**, *6*, 1565−1577.
(32) Pellegrino, T.; Manna, L.; Kudera, S.; Liedl, T.; Koktysh, T.; Rogach, A. L.; Keller, S.; Radler, J.; Natile, G.; Parak, W. J. *Nano Lett.* **2004**, *4*, 703−707.
(33) Muir, B. W.; Moffat, B. A.; Harbour, P.; Coia, G.; Zhen, G.; Waddington, L.; Scoble, J.; Krah, D.; Thang, S. H.; Chong, Y. K.; Mulvaney, P.; Hartley, P. *J. Phys. Chem. C* **2009**, *113*, 16615−16624.
(34) Riedinger, A.; Zhang, F.; Dommershausen, F.; Rocker, C.; Brandholt, S.; Nienhaus, G. U.; Koret, U.; Parak, W. J. *Small* **2010**, *6*, 2590−2597.
(35) Tamang, S.; Beaune, G.; Texier, I.; Reiss, P. *ACS Nano* **2011**, *5*, 9392−9402.
(36) Chen, Y.; Chi, Y.; Wen, H.; Lu, Z. *Anal. Chem.* **2007**, *79*, 960−965.
(37) Josephson, L.; Kircher, M. F.; Mahmood, U.; Tang, Y.; Weissleder, R. *Bioconjugate Chem.* **2002**, *13*, 554−560.
(38) Liu, W.; Howarth, M.; Greytak, A. B.; Zheng, Y.; Nocera, D. G.; Ting, A. Y.; Bawendi, M. G. *J. Am. Chem. Soc.* **2008**, *130*, 1274−1284.
(39) Major, J. L.; Meade, T. J. *Acc. Chem. Res.* **2009**, *42*, 893−903.
(40) Que, E. L.; Chang, C. J. *Chem. Soc. Rev.* **2010**, *39*, 51−60.
(41) Low, P. S.; Henne, W. A.; Doorneweerd, D. D. *Acc. Chem. Res.* **2008**, *41*, 120−129.
(42) Lu, Y. J.; Low, P. S. *Adv. Drug Delivery Rev.* **2002**, *54*, 675−693.
(43) Bharali, D. J.; Lucey, D. W.; Jayakumar, H.; Pudavar, H. E.; Prasad, P. N. *J. Am. Chem. Soc.* **2005**, *127*, 11364−11371.
(44) Vlahov, I. R.; Leamon, C. P. *Bioconjugate Chem.* **2012**, *23*, 1357−1369.
(45) Wu, H.; Liu, G.; Zhang, S.; Shi, J.; Zhang, L.; Chen, Y.; Chen, F.; Chen, H. *J. Mater. Chem.* **2011**, *21*, 3037−3045.
(46) Kim, H. M.; Cho, B. R. *Acc. Chem. Res.* **2009**, *42*, 863−872.
(47) Knemeyer, J.-P.; Herten, D.-P.; Sauer, M. *Anal. Chem.* **2003**, *75*, 2147−2153.
(48) Setua, S.; Menon, D.; Asok, A.; Nair, S.; Koyakutty, M. *Biomaterials* **2010**, *31*, 714−729.
(49) Roy, I.; Ohulchanskyy, T. Y.; Pudavar, H. E.; Bergey, E. J.; Oseroff, A. R.; Morgan, J.; Dougherty, T. J.; Prasad, P. N. *J. Am. Chem. Soc.* **2003**, *125*, 7860−7865.
(50) Sato, K.; Yokosuka, S.; Takigami, Y.; Hirakuri, K.; Fujioka, K.; Manome, Y.; Sukegawa, H.; Iwai, H.; Fukata, N. *J. Am. Chem. Soc.* **2011**, *133*, 18626−18633.
(51) Warner, J. H.; Hoshino, A.; Yamanmoto, K.; Tilley, R. D. *Angew. Chem., Int. Ed.* **2005**, *44*, 4550−4554.
(52) Peng, C.; Hu, W.; Zhou, Y.; Fan, C.; Huang, Q. *Small* **2010**, *6*, 1686−1692.
(53) Gollavelli, G.; Ling, Y. -C. *Biomaterials* **2012**, *33*, 2532−2545.
(54) Song, Y.; Xu, X.; MacRenaris, K. W.; Zhang, X. -Q.; Mirkin, C. A.; Meade, T. J. *Angew. Chem., Int. Ed.* **2009**, *38*, 9143−9147.
(55) Park, J.; Nam, J.; Won, N.; Jin, H.; Jung, S.; Jung, S.; Cho, S. -H.; Kim, S. *Adv. Funct. Mater.* **2011**, *21*, 1558−1566.